

Methane Oxidation over PdO: Towards a Better Understanding of the Influence of the Support Material

Kevin Keller,^[a] Patrick Lott,^{*[a]} Steffen Tischer,^[b] Maria Casapu,^[a] Jan-Dierk Grunwaldt,^[a, b] and Olaf Deutschmann^[a, b]

The presence of water vapor during the oxidation of the strong greenhouse gas methane over PdO-based catalysts is known to result in severe inhibition and catalyst deactivation. In this context, our current study elucidates the role of the support material for different water concentrations in the reaction gas mixture. Compared to a reference PdO/Al₂O₃ catalyst, the catalytic activity can be significantly enhanced when using SnO₂ and ZrO₂ as support materials and remains stable during 24 h of

operation at 823 K in the presence of 12% H₂O, whereas under identical conditions CH₄ conversion drops by 68% over PdO/Al₂O₃. The interplay between Pd species and catalyst support was systematically characterized by thermogravimetric analysis, temperature-programmed reduction experiments and TEM measurements. Finally, a kinetic scheme was derived based on the experimental data.

Introduction

Due to their superior activity, PdO-based catalysts are inevitable for the control of methane (CH₄) emissions from natural gas engines.^[1] Although especially catalysts supported on alumina (Al₂O₃) exhibit high performance in the low-temperature regime,^[2] they suffer from severe catalyst deactivation in the presence of water (H₂O) vapor, which is an unavoidable species evolving during the combustion of hydrocarbons.^[3] Ciuparu et al.^[4] attributed the reduction of catalytic activity to hydroxyl formation on the catalytically active PdO surface, which occurs due to the interaction with H₂O molecules that are either produced during the catalytic oxidation process or that are adsorbed from the gaseous atmosphere. Furthermore, upon exposure to reaction gas mixtures, noble metal particles can undergo sintering processes.^[5] Since methane oxidation proceeds via a Mars-van-Krevelen mechanism,^[6] the catalytic rate is a complex function of the particle size. While the oxygen in bigger particles is more accessible in the oxidation process leading to increased turnover frequencies,^[6b,7] smaller noble metal particles offer larger surface area for reactant adsorption and reaction. In this context, Stakheev et al.^[7] found an optimized oxidation rate for particles with an average diameter of 4.2 nm for PdO-based catalysts supported on Al₂O₃. Although

PdO is claimed to be the most active species for CH₄ conversion in lean atmospheres, also metallic Pd can be active for C–H bond scission in the CH₄ molecule,^[8] which is supposed to be the rate-determining step during CH₄ conversion.^[9]

In order to overcome H₂O-induced deactivation, water inhibition is frequently investigated in combination with support material effects on the active noble metal particles during the catalytic combustion. Especially metal oxide support materials with a high oxygen mobility such as ceria (CeO₂)^[10] and zirconia (ZrO₂)^[11] can influence the re-oxidation of PdO particles^[12] and might help sustaining high catalytic activity especially in the presence of water.^[4,11,13] Therefore, among other factors, the overall oxygen mobility has been suggested a key aspect when mitigating water inhibition.^[3c] In particular, a higher stability of PdO/ZrO₂ was observed also in absence of additionally dosed water, which was attributed to the oxygen storage capacity of the support material ZrO₂.^[4] Additionally, tin oxide (SnO₂) was suggested as a feasible support material for catalysts exhibiting strong metal-support interactions and high water tolerance in the low-temperature regime.^[14] Since the hydroxylation behavior due to the hydrophilic or hydrophobic nature of the support material has been proposed to influence the water tolerance and long-term stability of methane oxidation catalysts,^[15] also zeolitic materials have been proposed as promising carriers for PdO. As emphasized by several recent research papers and review articles,^[16] mainly the Si/Al ratio in the zeolite framework and the corresponding support acidity seem to govern high catalytic activity and water tolerance, i.e. by stabilizing well-dispersed PdO particles. Moreover, recent work by Huang et al.^[17] and by Xiong et al.^[18] points to the possibility of optimizing the structure of the noble metal in order to maximize CH₄ conversion, either by introducing surface defects on the surface of the noble metal, which potentially increase the C–H bond activation,^[17] or by preparing water-tolerant two-dimensional PdOx rafts.^[18] These findings are encouraging on an academic level, however, such advanced preparation approaches may not allow a direct transfer into full-

[a] K. Keller, Dr. P. Lott, Dr. M. Casapu, Prof. Dr. J.-D. Grunwaldt, Prof. Dr. O. Deutschmann
 Institute for Chemical Technology and Polymer Chemistry (ITCP)
 Karlsruhe Institute of Technology (KIT)
 Engesserstr. 20, 76131 Karlsruhe (Germany)
 E-mail: patrick.lott@kit.edu

[b] Dr. S. Tischer, Prof. Dr. J.-D. Grunwaldt, Prof. Dr. O. Deutschmann
 Institute of Catalysis Research and Technology (IKFT)
 Karlsruhe Institute of Technology (KIT)
 Hermann-von-Helmholtz-Platz 1, 76344 Eggenstein-Leopoldshafen (Germany)

© 2023 The Authors. ChemCatChem published by Wiley-VCH GmbH. This is an open access article under the terms of the Creative Commons Attribution License, which permits use, distribution and reproduction in any medium, provided the original work is properly cited.

scale catalyst production that generally relies on simpler methods for easier upscaling.

Although in the past numerous studies investigated specific catalyst formulations and the influence of the support material in detail, a direct comparison of different catalyst systems is often difficult and not straightforward, since preparation methods, noble metal loading, reactor dimensions, flow characteristics, and gas composition differ. Besides, profound conclusions on the influence of the support material can only be drawn with unified conditions. A possible approach was already described in the literature by Mao et al.,^[19] utilizing atomic layer deposition (ALD) of metal oxides like NiO, Co₃O₄, CeO₂, or ZrO₂ onto γ -Al₂O₃ to receive different support material layers with well-defined physicochemical properties. The respective study shows how oxidation rates of carbon monoxide (CO) and CH₄ can be influenced by the layering approach, however, this is not sufficient to capture the complete metal-support interaction from preparation to catalysis itself. In addition to experimental data on the water inhibition effect and the influence of the support material on Pd-based methane oxidation catalysts, microkinetic models can help to further understand these phenomena and facilitate catalyst development. Modern microkinetic models for reduced Pd catalysts in fuel-rich mixtures^[20] and for oxidized PdO particles under lean conditions^[9] already allow for describing the contribution of both palladium phases to the methane oxidation, including the transition between reduced and oxidized Pd during heating and cooling cycles. However, such simulations are limited by their chosen theoretical background method, i.e. the mean-field approximation, and therefore can only be formulated for a given type of catalytic activity and support material. In order to overcome these boundaries, both the experimental foundation and the simulation of these phenomena need to be improved. Although global kinetics are mostly limited to the described setup environment they are developed for, their formulation allows to capture and compare the frequently studied water effects on methane oxidation over different support materials typically with higher cost and time efficiency than microkinetic models.^[21]

This work aims at deepening the understanding of the total methane oxidation and underlying water inhibition effect on PdO-based catalysts. For this, powder-bed experiments with Pd-catalysts supported on Al₂O₃, CeO₂, SnO₂, and ZrO₂ were conducted in the absence and presence of steam, which provides a solid database for discussing the water inhibition effect. Particle size and surface analysis of the catalyst samples as well as thermogravimetric analysis (TGA) and temperature-programmed reduction (TPR) measurements allow to correlate structural information with the dynamic transient behavior of the catalysts during operation. Subsequently, global kinetics are used within a reactor model to simulate the water inhibition effect and influence of the support material for the packed bed experiments, showcasing the general applicability of the chosen formulation. The results presented herein can help to understand and improve PdO-based catalysts for methane oxidation and are of particular interest for future development of models aiming at simulating the presented dynamic effects that need a

broad range of experimental results and structural information, as well as surface processes during the oxidation process.

Results and Discussion

Catalytic activity during light-off

Since alumina-supported PdO catalysts are well established and widely studied in the context of methane oxidation, PdO/Al₂O₃ serves as a reference catalyst regarding catalytic activity and water inhibition throughout this study. Figure 1 summarizes the CH₄ conversion during light-off in a reaction gas mixture consisting of 3200 ppm CH₄, 10% O₂ in N₂ in absence and presence of 1–12% H₂O. In a dry environment, PdO/Al₂O₃ achieves 50% CH₄ conversion at 580 K (T₅₀) and 90% conversion (T₉₀) at 609 K. While the presence of only 1% H₂O of water in the feed gas stream shifts the light-off curve dramatically towards higher temperatures, namely to 640 K for T₅₀ and 686 K for T₉₀, the water inhibition effect further increases with increasing H₂O content, e.g. resulting in a T₅₀ of 699 K with 6% H₂O and a T₅₀ of 725 K at 12% H₂O. This continuous inhibition is predominantly caused by active sites being blocked by hydroxyl groups originating from the feed gas.^[5d] Altering the support material, e.g. by using materials with improved oxygen mobility, has been reported to enhance the initial catalytic activity^[4,11,13] and mitigate the pronounced water inhibition effect. Using CeO₂ as a support material, for instance, changes the oxidation behavior of the catalyst as depicted in Figure 1b. Compared to PdO/Al₂O₃, the catalytic conversion of methane under dry conditions over PdO/CeO₂ is shifted by 45 K towards higher temperatures at 50% conversion. However, although the catalyst performance is worse compared to the alumina-supported reference catalyst, the water inhibition effect is overall less pronounced, i.e. a T₅₀ of 666 K was found in the presence of 6% H₂O over PdO/CeO₂, which is 33 K lower than for the PdO/Al₂O₃ reference catalyst. The higher activity is also maintained at elevated temperatures and 12% H₂O being present in the stream with a final T₉₀ of 712 K, which is 31 K lower than for PdO/Al₂O₃. Despite the comparably low surface area of the support material (c.f. Table 2), the data shown in Figure 1c for PdO/SnO₂ show a similar trend. With T₅₀ and T₉₀ of 585 K and 623 K, respectively, under dry reaction conditions, values close to those measured for the highly active Al₂O₃-supported reference catalyst are found. Although the initial water inhibition is more pronounced compared to the CeO₂-supported sample when the steam concentration is increased to 1%, higher methane oxidation rates are measured within the complete range of externally dosed water concentrations. At 6% H₂O, T₅₀ is found to be 656 K, whereas 90% conversion is achieved at 688 K and therefore 42 K lower compared to PdO/Al₂O₃. The superior activity is also maintained at a higher water concentration of 12%, with T₅₀ and T₉₀ of 675 K and 708 K respectively. In line with previous research,^[22] PdO/ZrO₂ exhibits a good initial activity in the absence of water at a similar level as the samples supported on Al₂O₃ and SnO₂. Again, high methane oxidation rates are observed over the whole range of

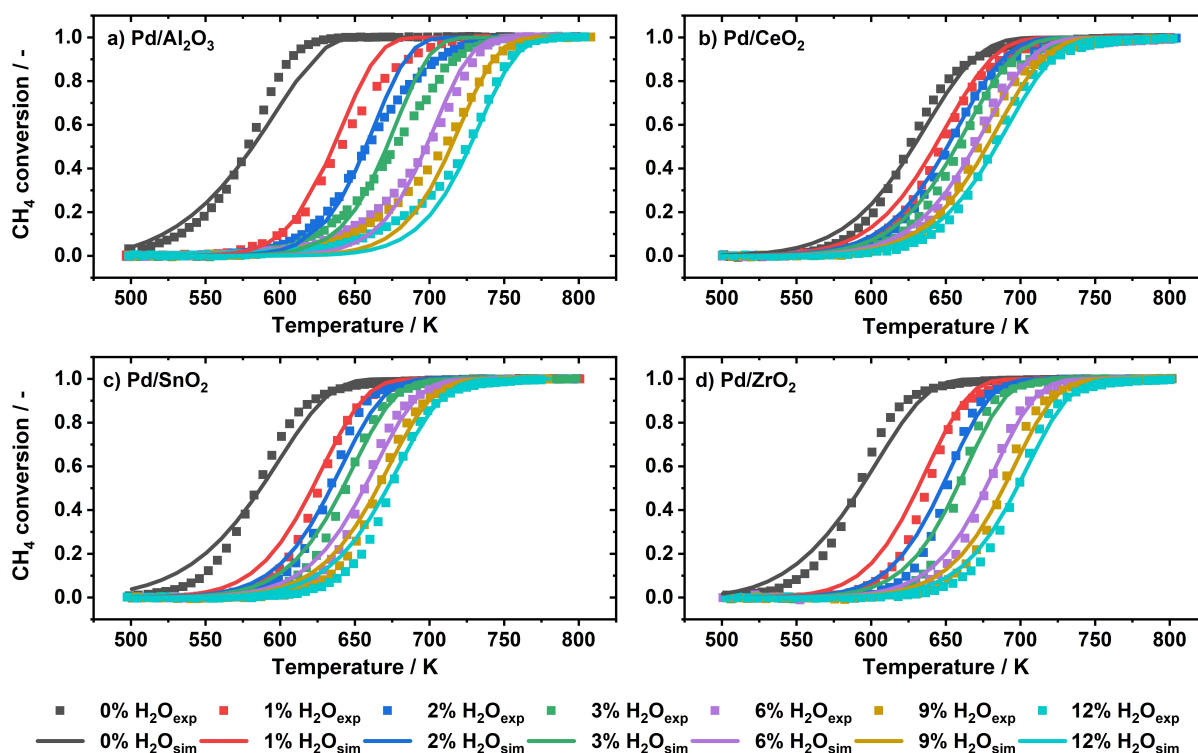


Figure 1. Different light-off measurements (dots) for PdO catalysts supported on a) Al₂O₃, b) CeO₂, c) SnO₂, and d) ZrO₂ as well as the corresponding simulations (lines) in 3200 ppm CH₄, 10% O₂ and balance N₂ in the absence and in the presence of different water concentrations. Temperature ramp = 3 K min⁻¹;

water concentrations, showing how the chosen support material can beneficially influence the catalytic performance of the noble metal particles.

Simulation results

The measurements presented above are captured within global kinetic simulations that incorporate the water inhibition effect tailored to the different support materials. The formation of H₂O during the oxidation process on the surface of the catalyst is known to directly block surface active sites of PdO, which are then unavailable during the Mars-van-Krevelen mechanism, as already shown by microkinetic models.^[5d,9] However, a deconvolution of the noble metal-related reaction pathways and the influence of the support material on the active noble metal particles during this inhibition mechanism is almost impossible within the range of the mean-field approximation that is typically used for microkinetic simulations. In contrast, global kinetics rather capture overall trends without accounting for different inhibition mechanisms either related to the active sites or the support, which ultimately allows a fairly good description of methane oxidation catalyst formulations in the presence of water.

For the simulations carried out, assuming a reaction rate order of zero with respect to oxygen, a modified Arrhenius type expression is used that defines the rate constant r_{CH_4} according to Eq. 1, with c_{CH_4} as methane concentration, A_0 as the

preexponential Arrhenius factor, $E_{a,0}$ as activation energy, and l as inhibition factor. The inhibition factor l allows to account for the water inhibition by considering the water concentration $c_{\text{H}_2\text{O}}$, the reaction order β , a second preexponential factor A_1 , and the corresponding activation energy $E_{a,1}$ according to Eq. 2.

$$-r_{\text{CH}_4} = A_0 \frac{e^{-\frac{E_{a,0}}{RT}} c_{\text{CH}_4}}{l} \quad (1)$$

$$l = 1 + A_1 e^{-\frac{E_{a,1}}{RT}} c_{\text{H}_2\text{O}}^\beta \quad (2)$$

Further details on the methodology can be found in the Experimental Section. The simulation results are shown in Figure 1 denoted as solid lines in comparison to the experimental results depicted with dots. The associated parameters of the global kinetic formulation are listed in Table 1. The model is clearly able to represent the experimental activity data for the entire temperature range. For instance, the light-off curve in

Table 1. Associated parameters of the global kinetic formulation for the different catalysts.

Catalyst	PdO/Al ₂ O ₃	PdO/CeO ₂	PdO/SnO ₂	PdO/ZrO ₂
A_0	1.30E+11	1.15E+07	4.48E+08	8.32E+08
$E_{a,0}/\text{kJ mol}^{-1}$	144	117	117	128
A_1	0.374	0.053	1.612	0.243
$E_{a,1}/\text{kJ mol}^{-1}$	-45	-23	-22	-30
β	1.99	0.92	0.87	1.27

absence of water over PdO/Al₂O₃ is well described with the parameters presented in Table 1. The introduction of the order of reaction with respect to water, β , in combination with the lumped-in inhibition kinetics allows to predict the shift in catalytic activities towards higher temperatures in the presence of different amounts of externally dosed water fairly well. A rather high activation energy $E_{a,0}$ of around 144.3 kJ mol⁻¹ and an order of water inhibition of -1.99 are used within the model for the PdO/Al₂O₃ catalyst. As already described above, the alumina-supported sample shows a pronounced immediate inhibition upon addition of water to the feed gas stream. From a model point of view, the combination of a high reaction order with respect to water and a water adsorption enthalpy value of -44.9 kJ mol⁻¹ explains the drop in catalytic activity in the presence of water.

The latter could imply strong interactions between adsorbed water on the surface with catalytically active sites, thus resulting in higher coverages by H₂O and the shift towards higher temperatures. On the other hand, a low initial activation energy and order of water inhibition is found for the PdO/CeO₂ catalyst with a final value of 116.7 kJ mol⁻¹ and -0.92 , respectively, accounting for the rather flat CH₄ oxidation light-off curves and the comparably small water inhibition effect. A combination of both, high initial dry activity and an order of reaction with respect to water close to 1 are found for the samples supported on SnO₂ and ZrO₂. In the presence of 12% H₂O, PdO/SnO₂ shows the best performance, which is represented by an order of water inhibition of -0.92 in the model and among the samples investigated herein the lowest water adsorption enthalpy of -22.2 kJ mol⁻¹. Additionally, with a value of 117.1 kJ mol⁻¹ the activation energy used for describing methane oxidation over Pd/SnO₂ is low in comparison, for instance, to 127.5 kJ mol⁻¹ that are used for PdO/ZrO₂. However, the model assumes a higher A_0 value for the latter catalyst, resulting in similar catalytic activities with respect to different water concentrations. The reported values are in good agreement with previous research using similar catalyst formulations. Depending on the PdO facet, i.e. PdO(100) or PdO(110), different activation energies between 125 and 160 kJ mol⁻¹ were determined,^[23] which changed to 150 kJ mol⁻¹ once PdO was supported on Al₂O₃,^[23a,24] with corresponding reaction orders with respect to water of -1.3 to -0.9 .^[25] Despite a lower noble metal loading than our present catalyst samples, Kikuchi et al.^[14b] reported an activation energy of 111 kJ mol⁻¹ for their 1.1 wt.% PdO/SnO₂ catalyst, which is also in good accordance to values recently reported by Hayes et al.^[26] Additionally, their H₂O adsorption enthalpy of -31 kJ mol⁻¹ on the SnO₂ supported catalyst and -49 kJ mol⁻¹ for the PdO/Al₂O₃ catalyst is in good agreement with our findings. Depending on the loading, activation energies between 172 and 185 kJ mol⁻¹ and a reaction order with respect to water of -1 for temperatures up to 700 K were found for PdO/ZrO₂ catalysts.^[15b,23a,24a,27] In combination, lower water adsorption enthalpies and a corresponding lower inhibition order with respect to water could lead to less hydroxyl formation on both the active noble metal particles as well as the support material and thus explain the higher methane oxidation rates.

Long-term activity tests

As already discussed in the previous sections, especially PdO-based catalysts supported on Al₂O₃ suffer from an instant inhibition in the presence of water. However, additional deactivation phenomena such as further hydroxyl-accumulation as well as sintering of active particles occur during long-term operation.^[5d] Figure 2 compares the light-off measurements that were conducted with degreened powder catalysts and samples that were operated for 24 h at 823 K in a reaction gas mixture containing 3200 ppm CH₄, 10% O₂, 12% H₂O, and bal. N₂. The aging and deactivation of the catalysts is clearly most pronounced for PdO/Al₂O₃. While the fresh sample was able to fully oxidize CH₄ at around 723 K, the aged catalyst converts only 32% CH₄ at the same temperature, which we predominantly attribute to a hydroxylation of the catalyst surface. Velin et al.^[28] identified two routes for this hydroxylation process, i.e. spillover effects near the PdO/Al₂O₃ boundary as well as adsorption and subsequent dissociation of water originating from the gas phase. Since only minor to moderate sintering was observed for PdO-based catalysts,^[5d,29] deactivation effects take place mainly on the surface of the catalyst.^[30] Similar effects have been reported before,^[31] focusing on light-off and consecutive light-out measurement. Inhere, the transient behavior of the catalytic activity was also explained with an immediate inhibition effect and a subsequent slow deactivation over time due to the accumulation of hydroxyl groups. While at higher temperatures the overall catalytic activity in absence and presence of water is similar, differences are most pronounced at lower temperatures, which was attributed to a rather slow H₂O desorption from the surface of the catalyst.^[4,8a,c] The simulation results already suggested a higher impact of the reaction order with respect to water as well as the highest negative adsorption enthalpy for alumina-supported samples, thus leading to a pronounced accumulation of adsorbed H₂O on the surface over time. Following the conclusions of the model based on smaller water adsorption enthalpies and orders of water inhibition, the other catalysts should in theory be less affected by long-term deactivation and hydroxyl accumulation from externally dosed water. These model-based predictions are in line with the trends observed during our measurement campaign (Figure 2). For PdO/CeO₂ the catalytic activity is slightly decreasing over time, leading to a shift of T_{50} by 24 K from 679 K to 703 K. However, full conversion of methane is still achieved within the studied temperature range. The catalytic samples supported on SnO₂ and ZrO₂ barely suffer from long-term deactivation and the light-off curves before and after the 24 h of aging match fairly well with regard to the starting point of the ignition, T_{50} , and the end of the temperature ramp, indicating the small effect of water on the active particles on larger time scales. Both phenomena are in line with studies conducted by Kikuchi et al.,^[14b] who reported material-dependent water adsorption enthalpies and consequently varying hydroxyl-formation tendencies, and experiments by Schwartz et al.^[8c,32] illustrating how support material-assisted oxygen exchange is hindered on Al₂O₃, hence leading to lower catalytic activities as compared to our other results. The latter is supposed to be a crucial factor in

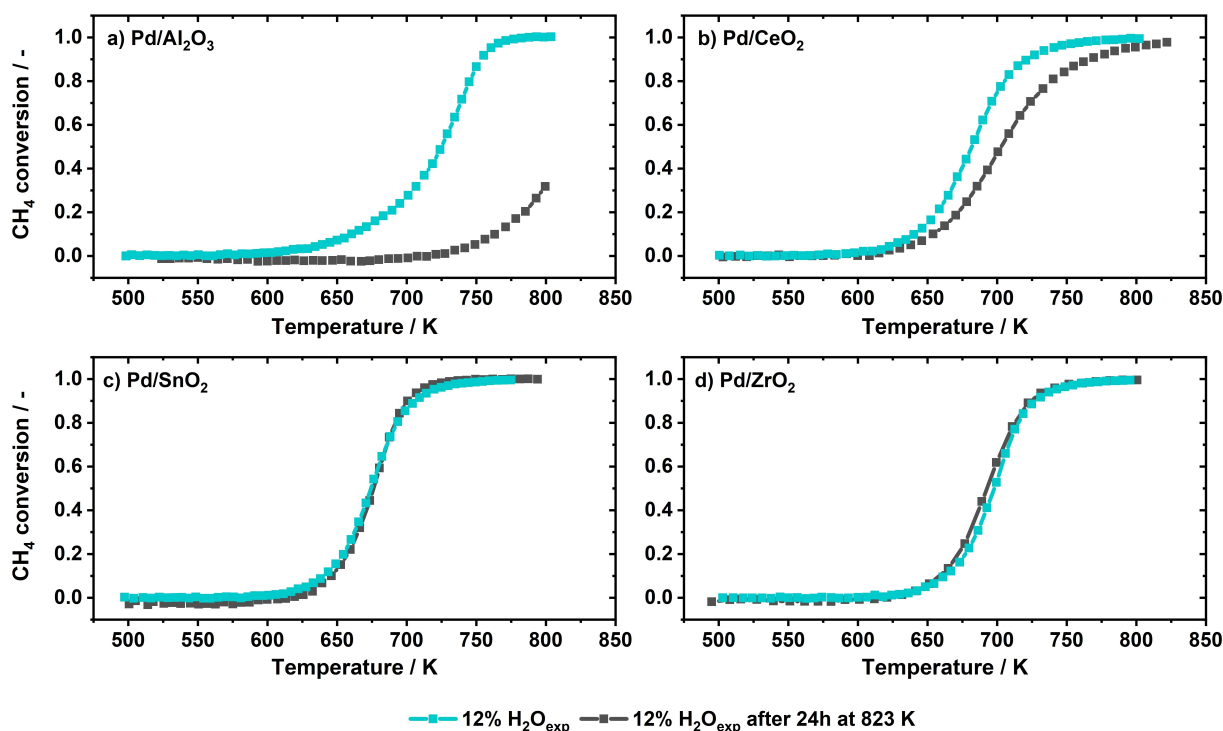


Figure 2. Initial light-off measurements (blue) for PdO catalysts supported on Al₂O₃, CeO₂, SnO₂, and ZrO₂ in 3200 ppm CH₄, 12% H₂O, 10% O₂ and balance N₂ with a temperature ramp of 3 K min⁻¹, compared to the light-off activity after 24 h in the described reactive gas atmosphere at 823 K. GHSV = 80,000 h⁻¹.

maintaining catalytic activity especially in presence of water.^[4,8c] For the PdO/SnO₂ sample the support material facilitates oxygen activation,^[33] hereby improving the methane oxidation also on longer time scales. On the other hand, for the PdO/ZrO₂ catalyst the noble metal-support interaction leads to an inhibition of hydroxyl accumulation on the surface of the noble metal and an increase in oxygen mobility, i.e. improved reducibility within the PdO-phase.^[34] Especially the mentioned reducibility of PdO-particles can strongly correlate with the measured catalytic activity, since the Mars-van-Krevelen mechanism involves a Pd/PdO redox cycle.^[6] The varying PdO particle size, which is discussed in more detail in the following section, might be another factor influencing the catalytic activity. Although under the conditions chosen for the present study deactivation effects due to sintering are of only minor importance, the noble metal particle size might be influential especially in the presence of water.^[5a] Their compared to the Al₂O₃-based reference sample larger noble metal particle size (c.f. Table 2) could somewhat favor the catalytic samples supported on SnO₂ and ZrO₂ in terms of water resistance. For this reason, the catalytic activity for CH₄ oxidation over PdO-based catalyst should always be evaluated in the context of the

chosen support material and its impact on the active noble metal particles.

Influence of the support material

The last part of this study focuses on experiments that are able to capture and measure differences in the behavior of the noble metal particles, thus explaining the influence of the chosen support material on an atomic level. While the water inhibition effect could be described mostly by the global kinetics relying on a combination of energy barriers for the initial methane oxidation, water adsorption enthalpies, and the order of reaction with respect to H₂O, the support material can additionally influence the dynamics of the noble metal particles on the surface of the catalyst. Since the CH₄ oxidation reaction follows the Mars-van-Krevelen mechanism,^[6b-d] the redox behavior of PdO species is particularly important. Although the dissociative adsorption of methane on the surface of the noble metal particles is presumably the rate-determining step in the oxidation process,^[14b] facile PdO reduction and re-oxidation steps are essential for a good and sustainable catalytic conversion, in which C–H activation involves lattice oxygen from PdO. As previously reported, under lean reaction conditions PdO is considered catalytically more active than Pd.^[9,20,35]

TGA was exploited to probe the influence of the carrier material on the noble metal redox dynamics. The thermodynamically driven auto-reduction of PdO to Pd at elevated temperatures was monitored for the different catalysts in an

Table 2. Noble metal particle size diameter according to STEM/EDXS images and dispersion using the hemispherical particle assumption.^[1b]

Catalyst	PdO/Al ₂ O ₃	PdO/CeO ₂	PdO/SnO ₂	PdO/ZrO ₂
Diameter/nm	1.7 ± 0.4	3.1 ± 0.8	4.1 ± 1.2	5.1 ± 1.6
Dispersion/%	65	36	27	21

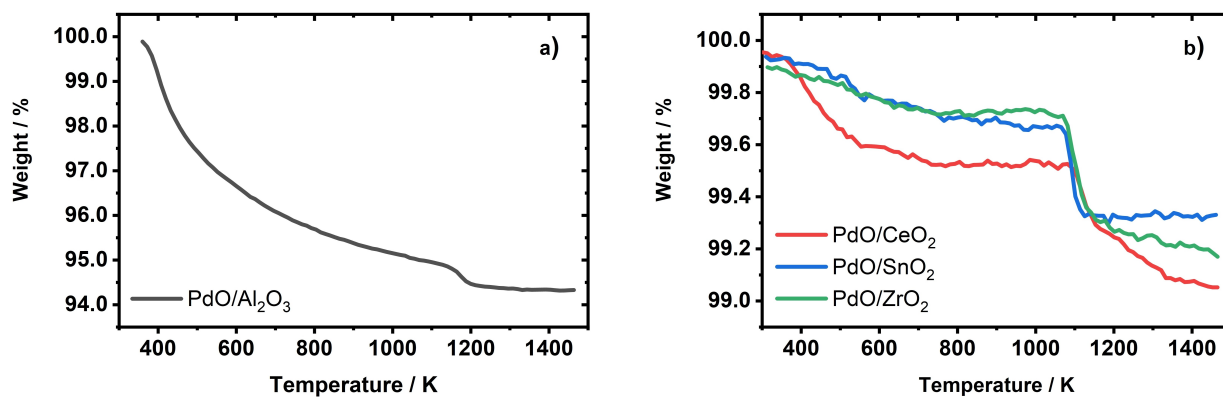


Figure 3. Mass loss during TGA for a) PdO/Al₂O₃ and b) for PdO catalysts supported on CeO₂, SnO₂, and ZrO₂ during the heating phase of 10 K min⁻¹ in 10% O₂ in Ar with a total flow rate of 100 ml min⁻¹.

oxidative gas mixture, which mimics the conditions present during the light-off tests. Figure 3 depicts the mass loss of all four samples during a heating ramp in 10% O₂/N₂ with 10 K min⁻¹. Due to the high surface area, the PdO auto-reduction onset on the highly hygroscopic support material Al₂O₃ was observed around 1150 K upon significant water desorption (Figure 3a). The influence of the other support materials on the dynamics of the PdO–Pd transformation is visible in Figure 3b. Inhere, the auto-reduction of PdO particles supported on CeO₂, ZrO₂, and SnO₂ occurred at a lower temperature of approximately 1073 K. These results are in good accordance with our catalytic data as well as the experiments conducted by Farrauto et al.^[36] A lower auto-reduction temperature implies a lower oxygen binding strength in the PdO particles, which means that the contribution of lattice-oxygen to the Mars-van-Krevelen mechanism is more likely even in the presence of excess oxygen, particularly at elevated temperatures. Since the PdO–Pd dynamics might change in the presence of a reductant, i.e. H₂ or CH₄, temperature-programmed reduction (TPR) experiments were conducted in the presence of 10% H₂/N₂ as depicted in Figure 4. In order to account for both, the reduction of the noble metal and of the support material, a temperature range of 270 K to 860 K was chosen for the H₂-TPR experiments. Herein, all catalytic samples show a negative H₂ peak at around 332 K, indicating the release of pre-adsorbed hydride species from the reduced Pd surface,^[37] whereas the main H₂ consumption peaks regarding the PdO–Pd reduction are found below 288 K. The PdO/Al₂O₃ catalyst shows the peak with the highest measured temperature of 285 K, similar to other measured catalysts supported on Al₂O₃.^[38] PdO-reduction on CeO₂ and ZrO₂ are measured at a comparable temperature of 283 K, whereas the SnO₂-supported catalyst shows the lowest reduction temperature of 275 K. In this regard, the surface reduction of SnO₂ starts at 473 K, with subsequent bulk reduction after 673 K as already described in the literature.^[39]

In principle, the highly reducible support material SnO₂ as shown in the TPR-measurement could influence the PdO/Pd particles and thus their stability in the presence of a reducing

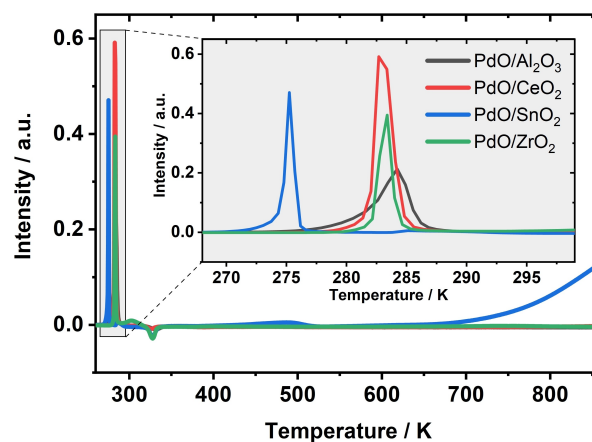


Figure 4. TPR profiles obtained from experiments with a temperature ramp of 10 K min⁻¹ in 10% H₂ in Ar. The inset shows the detailed H₂ consumption peak of the PdO reduction between 270 K and 290 K.

agent, explaining the early offset of the measured reduction.^[33b] Low-temperature TPR measurements are particularly suitable for uncovering such phenomena that are induced by only small temperature differences, since such effects diminish at the higher temperatures during the TGA measurements. The stability trends that were found for the PdO-particles during the TGA and TPR experiments show a similar correlation with the CH₄ oxidation activity observed in the light-off experiments,^[10c] namely PdO on ZrO₂ and SnO₂ being more active compared to PdO/Al₂O₃. Thus, our characterization data can help to accurately describe and quantify the influence of the support material in general.

However, since for understanding the catalytic activity the average noble metal particle diameter is of high importance as well, the PdO particle sizes were determined by means of scanning transmission electron microscopy (STEM). In addition, energy dispersive X-ray spectroscopy (EDXS) helped to precisely identify noble metal particles on the oxidic support materials. For each catalyst formulation, one representative STEM image is shown in Figure 5. The mean noble metal particle size

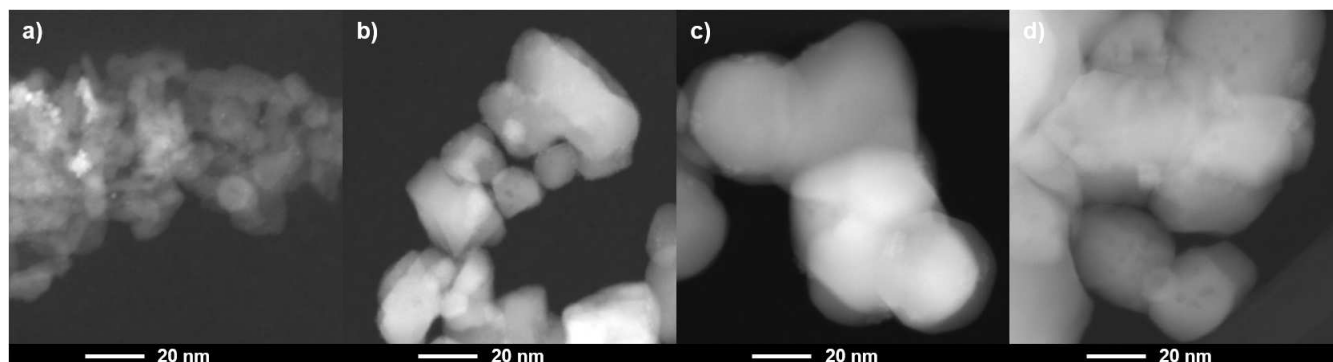


Figure 5. STEM images of the freshly prepared catalyst samples, a) PdO/Al₂O₃, b) PdO/CeO₂, c) PdO/SnO₂, and d) PdO/ZrO₂.

diameters as summarized in Table 2 were obtained by analyzing at least 150 noble metal particles for each sample.

The biggest PdO particles with a mean diameter of 5.1 nm are found for the ZrO₂ supported catalyst, followed by the sample supported on SnO₂ with a mean particle diameter of 4.1 nm. The smallest noble metal particles are found on Al₂O₃. These findings suggest that the TPR-signal measured for the PdO/SnO₂ catalyst at low temperatures is not simply caused by the size of the active particles for which bigger particles are more reduced at comparably lower temperatures, but is also highly influenced by potentially strong noble metal-support interactions influencing the catalytic conversion of methane.^[40]

On the one hand, small particles are desirable to maximize the catalytically active surface area. On the other hand, the turnover frequency (TOF) for CH₄ oxidation increases with the particle size of PdO-based catalysts,^[7,41] which is due to the fact that oxygen in larger particles is less strongly bound to the structure^[27] and its participation in the catalytic conversion is consequently more likely. However, the TOF is also influenced by the support material and the presence of water as shown in Figure 6. Herein, the TOF for CH₄ conversion during the light-off experiments is plotted at 550 K for the H₂O-free reaction mixture and at 640 K in the presence of water. These temper-

atures were chosen to ensure comparable TOF values for all catalysts while maintaining low conversion rates so that differential conditions were fulfilled.^[7,41] In the absence of water, the ceria-supported sample, which has a mean particle size of 3.1 nm, exhibits the lowest TOF of only 0.064 s⁻¹. In contrast, PdO/Al₂O₃ with its lower (1.7 nm) and PdO/SnO₂ with its higher (4.1 nm) mean particle size have substantially higher TOFs (Figure 6), which points to a strong impact of the support material that additionally influences the catalytic activity. When examining the TOF values obtained in the presence of water, the catalyst supported on CeO₂ partly suppresses the inhibition effect of water on the catalytic activity. At the same time, the Al₂O₃-supported sample is the most affected by the presence of H₂O, exhibiting the lowest TOF. Hence, apart from the presence of slightly bigger noble metal particles, the oxygen storage capacity of the CeO₂ support material^[10] seems to help mitigating the water inhibition effect. For even larger noble metal particles, as present in PdO/SnO₂ and PdO/ZrO₂, a high catalytic activity is maintained also in the presence of water. While it was postulated that the overall TOF essentially linearly increases with increasing particle diameter,^[27,41] the support material can additionally influence the methane conversion rate what can be seen in particular in the case of PdO/CeO₂ and PdO/ZrO₂. In the absence of water, the TOF for PdO/SnO₂ is 18% and 94% higher than for PdO/ZrO₂ and PdO/CeO₂, respectively, despite the smaller particles on SnO₂ compared to the ZrO₂-based sample. However, the difference declines in the presence of water, which results in more similar TOFs for both catalysts, hereby suggesting different noble metal-support interactions, beyond simple particle size effects.

In summary, the influence of the particle size for methane oxidation as well as the importance and measurability of the support material effect including its surface area on the active noble metal particles in the complex redox process is undeniable and especially important to develop robust and active catalysts in presence of water.

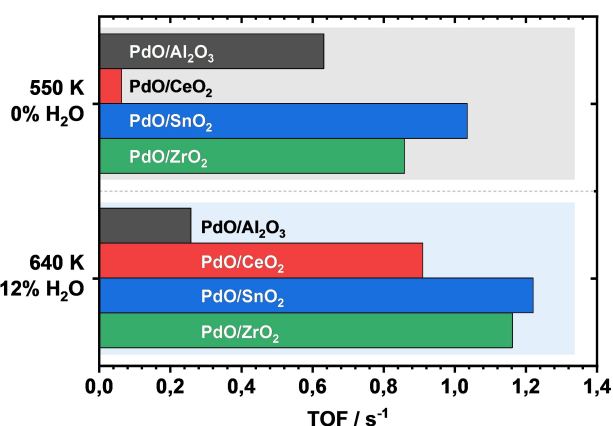


Figure 6. TOF at 550 K under dry (3200 ppm CH₄, 10% O₂, bal. N₂) and at 640 K under wet (3200 ppm CH₄, 10% O₂, 12% H₂O, bal. N₂) conditions.

Conclusion

The present study compares PdO-based methane total oxidation catalysts that were prepared on four different support materials. Initial activity tests underscored the high activity of PdO/Al₂O₃ catalysts, which however suffer from severe inhibition and long-term deactivation in the presence of water vapor. While keeping the noble metal loading constant, the use of CeO₂ as a support material leads to a smaller water inhibition and particularly SnO₂- and ZnO₂-based samples demonstrated superior CH₄ conversion rates in absence as well as in presence of water. Furthermore, global kinetic expressions were derived to describe the different catalysts. While PdO/CeO₂ showed the smallest water inhibition factor of -0.92 in comparison to -1.99 for PdO/Al₂O₃, smaller water adsorption enthalpies of 22.2 kJ mol⁻¹ and 30.0 kJ mol⁻¹ were found for PdO/SnO₂ and PdO/ZrO₂, respectively, which explains the better catalytic performance in the presence of water vapor and could thus be a key descriptor for designing novel catalyst formulations. Notably, this enhanced activity was even maintained during long-term activity tests that lasted 24 h. Over PdO/Al₂O₃, methane conversion dropped by more than 68% compared to its initial catalytic activity, whereas the other three systems were substantially less affected. While the light-off curve for PdO/CeO₂ after 24 h of aging was only shifted by about 24 K, the catalytic activity of PdO/ZrO₂ and PdO/SnO₂ was barely affected compared to the as-prepared samples.

Thermogravimetric (TG) measurements and temperature-programmed experiments were conducted to further explain the influence of the support material on the active noble metal particles. Although on average the biggest PdO particles were found for PdO/ZrO₂ with a diameter of 5.1 nm in comparison to 1.7 nm for PdO/Al₂O₃, TG measurements in excess oxygen (at elevated temperatures) and TPR experiments in the presence of H₂ uncovered that the PdO particles supported on SnO₂ (mean diameter of 4.1 nm) showed the highest redox activity. Our results suggest that the combined effect of particle size diameter with the direct impact on the TOF and the influence of the support material could account for higher methane oxidation rates, with the accessibility of lattice oxygen participating in the Mars-van-Krevelen mechanism as a key descriptor. The results presented in this study can not only help to further improve catalyst systems for methane oxidation, but can also ease the description of future catalyst formulations by means of cost- and time-efficient global kinetic models, particularly with respect to their water resilience.

Experimental Section

Catalyst preparation

Prior to the addition of noble metal, the support materials listed in Table 3 were calcined at 973 K in static air for 5 h. Afterwards, the catalyst powder samples with a target noble metal loading of 2.3 wt.% were prepared by incipient wetness impregnation (IWI) using an aqueous solution of (NH₃)₄Pd(NO₃)₂ (chemPUR, 5.0 wt.% Pd). Subsequently the sample was first dried at 343 K for 1 h and

Support	Manufacturer	BET-surface area [m ² g ⁻¹]	BET-pore volume [cm ³ g ⁻¹]
Al ₂ O ₃	SASOL	176	0.46
CeO ₂	MEL Chemicals	32.1	0.084
SnO ₂	Alfa Aesar	6.4	0.02
ZrO ₂	Alfa Aesar	6.0	0.015

then calcined at 823 K for 5 h. The target noble metal loading was confirmed by elemental analysis (inductively coupled plasma optical emission spectrometry, ICP-OES) to be between 2.23–2.28 for all the catalysts subject to this study.

Catalytic activity testing

The activity of the catalyst was studied in a quartz glass tubular reactor with an inner diameter of 8 mm containing 300 mg of the prepared powder catalyst. The catalyst was first sieved to a particle size fraction of 125–250 μm for minimal mass transfer limitation^[42] and subsequently diluted with 700 mg of sieved SiO₂ (sieve fraction 125–250 μm) for a good heat distribution inside the packed bed with a length of approximately 1.5 cm. Analogous to the setup and the measurement routine described in our previous publication,^[5d] gases were dosed with mass flow controllers (MFC, Bronkhost) and water vapor was dosed by a controlled evaporator and mixer system (CEM, Bronkhost). End-of-pipe gas concentrations were measured with a Fourier-transform infrared spectrometer (FTIR, Multigas MG2030, MKS). During the light-off measurements between 500 K and 823 K in a gas mixture consisting of 3200 ppm CH₄, 10% O₂ in N₂ and different H₂O amounts of up to 15%, a temperature ramp of 3 K min⁻¹ was achieved by means of Eurotherm controllers that regulated the furnace temperature. The temperature was measured with two thermocouples within the reactor right before and after the catalytic bed. High dilution of the reactants as well as an overall low flow rate ensure isothermal conditions. As illustrated in Figure 7, all catalyst samples were degreened for 1 h at 823 K in the reactive gas atmosphere in absence of water with a constant flow rate of 1 L min⁻¹ prior to the kinetic tests.

For the 24 h long-term activity tests in 3200 ppm CH₄, 10% O₂, 12% H₂O, and bal. N₂, the temperature was set to 823 K. After cool-down, the subsequent light-off was measured and compared with the initial catalytic activity. While the light-off tests were used to evaluate and investigate the initial activity of the catalyst formation and especially the instant inhibition by H₂O, the repetition after 24 h of aging allow uncovering aging and long-term deactivation processes developing on the different catalyst formulations. The CH₄ conversion shown in Figure 1 and 2 was calculated based on

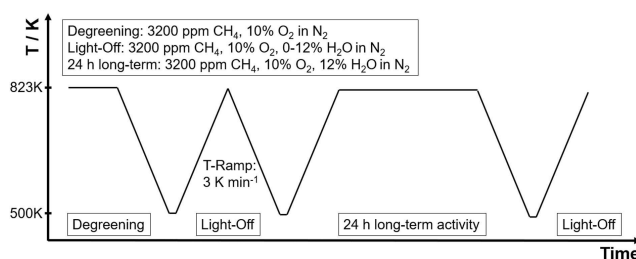


Figure 7. Reaction procedure comprising a degreening, the light-off test and the subsequent 24 h long-term activity test in the presence of 12% H₂O.

experimentally determined inlet and outlet concentrations and was further used for determining the turnover frequencies (TOF) given in Figure 6. The latter was calculated as defined in Eq. 3.^[43]

$$\text{TOF} = \frac{\dot{V} X_{\text{C}_0(\text{CH}_4)_p}}{\frac{RT}{m_{\text{PdO}}} D} \quad (3)$$

Inhere, \dot{V} is the volumetric flow rate with the conversion X of methane between 0 and 1. $c_0(\text{CH}_4)$ is the volumetric inlet concentration of CH_4 , p the pressure, R the gas constant and T the temperature in Kelvin. Additionally, m_{PdO} is the used weight of PdO, M_{PdO} is the molar weight, and D dispersion of the noble metal in the catalyst sample. The latter is calculated according to Eq. 4^[44] from the particle diameter D_{NP} that was obtained from the STEM images.

$$D = \frac{1.11}{D_{\text{NP}}} \quad (4)$$

Characterization techniques

Temperature-programmed reduction experiments with H_2 (H_2 -TPR) were conducted in an AutoChem II Chemisorption Analyzer (micromeritics),^[45] hereby providing information on the reducibility of both, the noble metal and support material. After fully oxidizing the catalyst sample (100 mg) for 10 min at 773 K with a temperature ramp of 10 K min^{-1} in 20% O_2 in N_2 , the sample is cooled to 193 K under 50 mL min^{-1} flow by means of a cryo-cooler. Ultimately, the subsequent temperature ramp from 193 K to 773 K (ramp rate 10 K min^{-1}) in 10% H_2 in Ar was monitored with a thermal conductivity detector (TCD), which allows to measure the hydrogen consumption as a function of temperature.

Thermogravimetric analysis (TGA) was performed in a STA 449 F3 Jupiter® (NETZSCH).^[46] Around 30 mg of the catalytic sample were put in a quartz glass crucible and exposed to a gaseous atmosphere containing 10% O_2 in N_2 with a total gas flow of 100 mL min^{-1} . Once the sample weight stabilized at 373 K, the measurement monitoring the weight of the catalyst sample was conducted with a temperature ramp of 10 K min^{-1} up to 1200 K.

Scanning transmission electron microscopy (STEM) images were obtained at the Laboratory for Electron Microscopy (LEM, KIT) using a FEI OSIRIS microscope operated with 200 kV electron energy. In addition, **energy dispersive X-ray spectroscopy (EDXS)** helped to identify the noble metal particle size whenever the contrast in the STEM images was low. From the obtained images, at least 150 particles per catalyst sample were analyzed using the software package Fiji to determine the final particle size of the noble metal particles.

Computational methods

The fixed bed flow reactor was numerically simulated using a 1D model, computationally realized by the DETCHEM^{PBR} code.^[47] No radial variations are assumed in the flow properties, resulting in a continuum modelling approach under steady-state isothermal conditions. The latter is justified by the low flow rate within the packed bed reactor, leading to only minor heat development even once complete methane oxidation rates are achieved at elevated temperatures. The present model solves continuity and species balance shown in Eq. 5 and 6 respectively.

$$\frac{d\rho u}{dz} = a_v \sum_{i \in S_g} M_i \dot{s}_i \quad (5)$$

$$\rho u \frac{dY_i}{dz} + Y_i a_v \sum_{i \in S_g} M_i \dot{s}_i = M_i (a_v \dot{s}_i + \dot{\omega}_i \varepsilon) \quad (6)$$

Inhere, ρ is the fluid phase density, z is the axial coordinate, u is the superficial velocity, a_v is the particle surface area to reactor volume ratio, \dot{s}_i is the surface phase reaction rate, M_i is the molar mass of species, Y mass fraction of gas phase species i , the fluid phase reaction rate $\dot{\omega}_i$, and the bed porosity ε . In the present study the model takes external fluid-solid mass transfer into account via the empirically derived fluid solid mass transfer coefficient k_{fs} as shown in Eq. 7. More details are described in an earlier publication from our group.^[48]

$$M_i \dot{s}_i = k_{i,fs} (\rho_{i,s} Y_{i,s} - \rho_i Y_i) \quad (7)$$

Kinetic model

A global power law expression was used to model the kinetics of the different catalyst formations, similar to the approach chosen in earlier studies for bimetallic Pd–Pt catalysts on Al_2O_3 .^[49] Herein, all experiments with various water concentrations were taken into account. As already described above, a modified Arrhenius-type expression is used that assumes a reaction rate order with respect to oxygen of zero (due to the vast excess oxygen under lean-burn conditions) and that can capture and reproduce the catalytic activity during the light-off measurements. For this, the rate constant equation r_{CH_4} considers the methane concentration c_{CH_4} as well as the Arrhenius parameters A_0 as the preexponential factor and the activation energy $E_{a,0}$ as denoted in Eq. 1. With the help of the inhibition factor I , as defined in Eq. 2, the water concentration $c_{\text{H}_2\text{O}}$ with the reaction order β is introduced and responsible for the simulated water inhibition effect. Since the H_2O concentration is directly considered in the rate constant via the inhibition factor I , the kinetic parameters listed in Table 1 remain the same for all water concentrations and only vary in dependence of the catalyst formulation.

$$-r_{\text{CH}_4} = A_0 \frac{e^{-\frac{E_{a,0}}{RT}} C_{\text{CH}_4}}{I} \quad (1)$$

$$I = 1 + A_1 e^{-\frac{E_{a,1}}{RT}} C_{\text{H}_2\text{O}}^\beta \quad (2)$$

Inhere, a second preexponential factor A_1 and activation energy $E_{a,1}$ regarding the water inhibition effect is defined. The kinetic parameters were fitted to experimental performance data of the specific catalyst/support system.

Acknowledgements

The authors thank M. Borchers (ITCP, KIT) for the H_2 -TPR measurements, S. Bastian (ITCP, KIT) for the N_2 -physisorption measurements, T. Bergfeldt (IAM-AWP, KIT) for the elemental analysis, and H. Störmer (LEM, KIT) for the TEM measurements. Furthermore, the authors thank Steinbeis GmbH für Technologietransfer (STZ 240 Reaktive Strömungen) for a cost-free licence of DETCHEMTM. The work was funded by the Deutsche Forschungsgemeinschaft (DFG,

German Research Foundation) via SFB 1441 – Project-ID 42688090. Open Access funding enabled and organized by Projekt DEAL.

Conflict of Interests

The authors declare no conflict of interest.

Data Availability Statement

The data that support the findings of this study are available from the corresponding author upon reasonable request.

Keywords: CH₄ oxidation · PdO-based catalysts · Effect of support material · Kinetics · Numerical simulation

- [1] a) O. Deutschmann, J.-D. Grunwaldt, *Chem. Ing. Tech.* **2013**, *85*, 595–617; b) A. Gremminger, J. Pihl, M. Casapu, J.-D. Grunwaldt, T. J. Toops, O. Deutschmann, *Appl. Catal. B* **2020**, *265*, 118571.
- [2] a) D. Ciuparu, M. R. Lyubovskiy, E. Altman, L. D. Pfefferle, A. Datye, *Catal. Rev.* **2002**, *44*, 593–649; b) P. Gélin, M. Primet, *Appl. Catal. B* **2002**, *39*, 1–37.
- [3] a) M. Alyani, K. J. Smith, *Ind. Eng. Chem. Res.* **2016**, *55*, 8309–8318; b) A. T. Gremminger, H. W. Pereira de Carvalho, R. Popescu, J.-D. Grunwaldt, O. Deutschmann, *Catal. Today* **2015**, *258*, 470–480; c) K. Persson, L. D. Pfefferle, W. Schwartz, A. Ersson, S. G. Järås, *Appl. Catal. B* **2007**, *74*, 242–250.
- [4] D. Ciuparu, E. Perkins, L. Pfefferle, *Appl. Catal. A* **2004**, *263*, 145–153.
- [5] a) T. W. Hansen, A. T. Delariva, S. R. Challa, A. K. Datye, *Acc. Chem. Res.* **2013**, *46*, 1720–1730; b) T. R. Johns, J. R. Gaudet, E. J. Peterson, J. T. Miller, E. A. Stach, C. H. Kim, M. P. Balogh, A. K. Datye, *ChemCatChem* **2013**, *5*, 2636–2645; c) X. Chen, Y. Cheng, C. Y. Seo, J. W. Schwank, R. W. McCabe, *Appl. Catal. B* **2015**, *163*, 499–509; d) K. Keller, P. Lott, H. Stotz, L. Maier, O. Deutschmann, *Catalysts* **2020**, *10*, 922.
- [6] a) J. Au-Yeung, K. Chen, A. T. Bell, E. Iglesia, *J. Catal.* **1999**, *188*, 132–139; b) C. A. Müller, M. Maciejewski, R. A. Koepfel, A. Baiker, *Catal. Today* **1999**, *47*, 245–252; c) D. Ciuparu, *Catal. Today* **2002**, *77*, 167–179; d) C. A. Müller, M. Maciejewski, R. A. Koepfel, R. Tschan, A. Baiker, *J. Phys. Chem.* **1996**, *100*, 20006–20014.
- [7] A. Y. Stakheev, A. M. Batkin, N. S. Teleguina, G. O. Bragina, V. I. Zaikovskiy, I. P. Prosvirina, A. K. Khudorozhkov, V. I. Bukhtiyarov, *Top. Catal.* **2013**, *56*, 306–310.
- [8] a) R. Burch, F. J. Urbano, *Appl. Catal. A* **1995**, *124*, 121–138; b) S. C. Su, J. N. Carstens, A. T. Bell, *J. Catal.* **1998**, *176*, 125–135; c) W. R. Schwartz, D. Ciuparu, L. D. Pfefferle, *J. Phys. Chem. C* **2012**, *116*, 8587–8593; d) Y. Mahara, K. Murata, K. Ueda, J. Ohyama, K. Kato, A. Satsuma, *ChemCatChem* **2018**, *10*, 3384–3387; e) A. Hellman, et al., *J. Phys. Chem. Lett.* **2012**, *3*, 678–682; f) Y.-H. C. Chin, C. Buda, M. Neurock, E. Iglesia, *J. Am. Chem. Soc.* **2013**, *135*, 15425–15442.
- [9] H. Stotz, L. Maier, A. Boubnov, A. T. Gremminger, J.-D. Grunwaldt, O. Deutschmann, *J. Catal.* **2019**, *370*, 152–175.
- [10] a) A. Trovarelli, *Catal. Rev.* **1996**, *38*, 439–520; b) J. Lee, T. H. Lim, E. Lee, D. H. Kim, *ChemCatChem* **2021**, *13*, 3706–3712; c) K. Murata, D. Kosuge, J. Ohyama, Y. Mahara, Y. Yamamoto, S. Arai, A. Satsuma, *ACS Catal.* **2020**, *10*, 1381–1387; d) S. Chen, et al., *ACS Catal.* **2021**, *11*, 5666–5677.
- [11] D. Ciuparu, F. Bozon-Verduraz, L. Pfefferle, *J. Phys. Chem. B* **2002**, *106*, 3434–3442.
- [12] a) C. E. Gigola, M. S. Moreno, I. Costilla, M. D. Sánchez, *Appl. Surf. Sci.* **2007**, *254*, 325–329; b) R. O. Fuentes, L. M. Acuña, A. G. Leyva, R. T. Baker, H. Pan, X. Chen, J. J. Delgado-Jaén, *J. Mater. Chem. A* **2018**, *6*, 7488–7499; c) D. Kaya, D. Singh, S. Kincal, D. Uner, *Catal. Today* **2019**, *323*, 141–147.
- [13] M. Cargnello, J. J. Delgado Jaén, J. C. Hernández Garrido, K. Bakhmutsky, T. Montini, J. J. Calvino Gámez, R. J. Gorte, P. Fornasiero, *Science* **2012**, *337*, 713–717.
- [14] a) H. Widjaja, K. Sekizawa, K. Eguchi, *BCSJ* **1999**, *72*, 313–320; b) R. Kikuchi, S. Maeda, K. Sasaki, S. Wennerström, K. Eguchi, *Appl. Catal. A* **2002**, *232*, 23–28.
- [15] a) R. Gholami, M. Alyani, K. Smith, *Catalysts* **2015**, *5*, 561–594; b) P. Araya, S. Guerrero, J. Robertson, F. J. Gracia, *Appl. Catal. A* **2005**, *283*, 225–233; c) Y. Liu, S. Wang, D. Gao, T. Sun, C. Zhang, S. Wang, *Fuel Process. Technol.* **2013**, *111*, 55–61.
- [16] a) H.-Y. Chen, J. Lu, J. M. Fedeyko, A. Raj, *Appl. Catal. A* **2022**, *633*, 118534; b) L. Wu, W. Fan, X. Wang, H. Lin, J. Tao, Y. Liu, J. Deng, L. Jing, H. Dai, *Catalysts* **2023**, *13*, 604; c) I. Friberg, A. H. Clark, P. H. Ho, N. Sadokhina, G. J. Smales, J. Woo, X. Auvray, D. Ferri, M. Nachtegaal, O. Kröcher, L. Olsson, *Catal. Today* **2021**, *382*, 3–12; d) A. W. Petrov, D. Ferri, F. Krumeich, M. Nachtegaal, J. A. van Bokhoven, O. Kröcher, *Nat. Commun.* **2018**, *9*, 2545; e) R. L. Mortensen, H.-D. Noack, K. Pedersen, S. Mossin, J. Mielby, *ChemCatChem* **2022**, *14*, e202101924.
- [17] W. Huang, A. C. Johnston-Peck, T. Wolter, W.-C. D. Yang, L. Xu, J. Oh, B. A. Reeves, C. Zhou, M. E. Holtz, A. A. Herzing, A. M. Lindenberg, M. Mavrikakis, M. Cargnello, *Science* **2021**, *373*, 1518–1523.
- [18] H. Xiong, D. Kunwar, D. Jiang, C. E. Garcia-Vargas, H. Li, C. Du, G. Canning, X. I. Pereira-Hernandez, Q. Wan, S. Lin, S. C. Purdy, J. T. Miller, K. Leung, S. S. Chou, H. H. Brongersma, R. ter Veen, J. Huang, H. Guo, Y. Wang, A. K. Datye, *Nat. Catal.* **2021**, *4*, 830–839.
- [19] X. Mao, A. Foucher, E. A. Stach, R. J. Gorte, *Catal. Lett.* **2019**, *149*, 905–915.
- [20] H. Stotz, L. Maier, O. Deutschmann, *Top. Catal.* **2017**, *60*, 83–109.
- [21] P. Lott, O. Deutschmann, *Proc. Combust. Inst.* **2022**.
- [22] J.-H. Park, J. H. Cho, Y. J. Kim, E. S. Kim, H. S. Han, C.-H. Shin, *Appl. Catal. B* **2014**, *160–161*, 135–143.
- [23] a) G. Zhu, J. Han, D. Y. Zemlyanov, F. H. Ribeiro, *J. Am. Chem. Soc.* **2004**, *126*, 9896–9897; b) R. Monteiro, D. Zemlyanov, J. Storey, F. Ribeiro, *J. Catal.* **2001**, *199*, 291–301.
- [24] a) F. H. Ribeiro, M. Chow, R. A. Dallabetta, *J. Catal.* **1994**, *146*, 537–544; b) S. T. Kolaczowski, W. J. Thomas, J. Titiloye, D. J. Worth, *Combust. Sci. Technol.* **1996**, *118*, 79–100; c) B. Liu, R. Hayes, M. Checkel, M. Zheng, E. Mirosh, *Chem. Eng. Sci.* **2001**, *56*, 2641–2658.
- [25] P. Hurtado, *Appl. Catal. B* **2004**, *51*, 229–238.
- [26] R. S. Kumar, R. E. Hayes, N. Semagina, *Chem. Eng. Sci.* **2023**, *269*, 118488.
- [27] K. Fujimoto, F. H. Ribeiro, M. Avalos-Borja, E. Iglesia, *J. Catal.* **1998**, *179*, 431–442.
- [28] P. Velin, M. Ek, M. Skoglundh, A. Schaefer, A. Raj, D. Thompsett, G. Smedler, P.-A. Carlsson, *J. Phys. Chem. C* **2019**, *123*, 25724–25737.
- [29] J.-D. Grunwaldt, N. van Vegten, A. Baiker, *Chem. Commun.* **2007**, 4635–4637.
- [30] X. Li, X. Wang, K. Roy, J. A. van Bokhoven, L. Artiglia, *ACS Catal.* **2020**, *10*, 5783–5792.
- [31] a) N. Sadokhina, F. Ghasempour, X. Auvray, G. Smedler, U. Nylén, M. Olofsson, L. Olsson, *Catal. Lett.* **2017**, *147*, 2360–2371; b) N. Sadokhina, G. Smedler, U. Nylén, M. Olofsson, L. Olsson, *Appl. Catal. B* **2017**, *200*, 351–360.
- [32] W. R. Schwartz, L. D. Pfefferle, *J. Phys. Chem. C* **2012**, *116*, 8571–8578.
- [33] a) Z. Zhao, B. Wang, J. Ma, W. Zhan, L. Wang, Y. Guo, Y. Guo, G. Lu, *Chin. J. Catal.* **2017**, *38*, 1322–1329; b) K. Sekizawa, H. Widjaja, S. Maeda, Y. Ozawa, K. Eguchi, *Appl. Catal. A* **2000**, *200*, 211–217.
- [34] Y. Wu, J. Chen, W. Hu, K. Zhao, P. Qu, P. Shen, M. Zhao, L. Zhong, Y. Chen, *J. Catal.* **2019**, *377*, 565–576.
- [35] P. Lott, P. Dolcet, M. Casapu, J.-D. Grunwaldt, O. Deutschmann, *Ind. Eng. Chem. Res.* **2019**, *58*, 12561–12570.
- [36] R. J. Farrauto, J. K. Lampert, M. C. Hobson, E. M. Waterman, *Appl. Catal. B* **1995**, *6*, 263–270.
- [37] a) H. Li, M. Shen, J. Wang, H. Wang, J. Wang, *Ind. Eng. Chem. Res.* **2020**, *59*, 1477–1486; b) C.-B. Wang, H.-K. Lin, C.-M. Ho, *J. Mol. Catal. A* **2002**, *180*, 285–291.
- [38] W. Lin, Y. Zhu, N. Wu, Y. Xie, I. Murwani, E. Kemnitz, *Appl. Catal. B* **2004**, *50*, 59–66.
- [39] T. Takeguchi, *Appl. Catal. A* **2003**, *252*, 205–214.
- [40] F. Gyger, A. Sackmann, M. Hübner, P. Bockstaller, D. Gerthsen, H. Lichtenberg, J.-D. Grunwaldt, N. Barsan, U. Weimar, C. Feldmann, *Part. Part. Syst. Charact.* **2014**, *31*, 591–596.
- [41] D. Roth, P. Gélin, A. Kaddouri, E. Garbowski, M. Primet, E. Tena, *Catal. Today* **2006**, *112*, 134–138.
- [42] G. Groppi, W. Ibashi, E. Tronconi, P. Forzatti, *Catal. Today* **2001**, *69*, 399–408.
- [43] J. Schütz, H. Störmer, P. Lott, O. Deutschmann, *Catalysts* **2021**, *11*, 300.

- [44] a) G. Ertl, H. Knözinger, F. Schüth, J. Weitkamp (Eds.) *Handbook of heterogeneous catalysis*, Wiley, Weinheim, **2008**; b) D. Chan, A. Gremminger, O. Deutschmann, *Top. Catal.* **2013**, *56*, 293–297.
- [45] M. Borchers, K. Keller, P. Lott, O. Deutschmann, *Ind. Eng. Chem. Res.* **2021**, *60*, 6613–6626.
- [46] M. Stehle, A. Gaur, S. Weber, T. L. Sheppard, M. Thomann, A. Fischer, J.-D. Grunwaldt, *J. Catal.* **2022**, *408*, 339–355.
- [47] O. Deutschmann, S. Tischer, S. Kleditzsch, V. Janardhanan, C. Correa, D. Chatterjee, N. Mladenov, H. D. Minh, H. Karadeniz, M. Hettel, V. Menon, A. Banerjee, H. Goßler, E. Daymo, A. B. Shirsath, DETCHEM Software package, 2.8 ed., www.detchem.com, Karlsruhe, **2022**.
- [48] S. Wan, K. Keller, P. Lott, A. B. Shirsath, S. Tischer, T. Häber, R. Suntz, O. Deutschmann, *Catal. Sci. Technol.* **2022**, *12*, 4456–4470.
- [49] a) B. Torkashvand, A. Gremminger, S. Valchera, M. Casapu, J.-D. Grunwaldt, O. Deutschmann, *SAE [Tech. Pap.]* **2017**, 01–1019; b) H. Dubbe, J. Schütz, O. Deutschmann, U. Nieken, *MTZ* **2017**, *78*, 82–85.

Manuscript received: March 7, 2023
Revised manuscript received: April 5, 2023
Accepted manuscript online: April 13, 2023
Version of record online: May 15, 2023